bioRxiv preprint doi: https://doi.org/10.1101/2021.02.18.431511; this version posted February 18, 2021. The copyright holder for this preprint (which was not certified by peer review) is the author/funder, who has granted bioRxiv a license to display the preprint in perpetuity. It is made available under aCC-BY 4.0 International license.

On the sensitivity analysis of porous finite element models for cerebral perfusion estimation

Józsa, T. I.*[1], Padmos, R. M.[2], El-Bouri, W. K.[1,3], Hoekstra, A. G.[2], and Payne, S. J.[1]

[1]Institute of Biomedical Engineering, Department of Engineering Science, University of Oxford, Parks Road, Oxford OX1 3PJ, UK
[2]Computational Science Laboratory, Institute for Informatics, Faculty of Science, University of Amsterdam, Science Park 904, Amsterdam 1098 XH, the Netherlands
[3]Liverpool Centre for Cardiovascular Science, Department of Cardiovascular and Metabolic Medicine, University of Liverpool, Thomas Drive, Liverpool L14 3PE, UK

Abstract

Computational physiological models are promising tools to enhance the design of clinical trials and to assist in decision making. Organ-scale haemodynamic models are gaining popularity to evaluate perfusion in a virtual environment both in healthy and diseased patients. Recently, the principles of verification, validation, and uncertainty quantification of such physiological models have been laid down to ensure safe applications of engineering software in the medical device industry. The present study sets out to establish guidelines for the usage of a three-dimensional steady state porous cerebral perfusion model of the human brain following principles detailed in the verification and validation (V&V 40) standard of the American Society of Mechanical Engineers. The model relies on the finite element method and has been developed specifically to estimate how brain perfusion is altered in ischaemic stroke patients before, during, and after treatments. Simulations are compared with exact analytical solutions and a thorough sensitivity analysis is presented covering every numerical and physiological model parameter.

The results suggest that such porous models can approximate blood pressure and perfusion distributions reliably even on a coarse grid with first order elements. On the other hand, higher order elements are essential to mitigate errors in volumetric blood flow rate estimation through cortical surface regions. Matching the volumetric flow rate corresponding to major cerebral arteries is identified as a validation milestone. It is found that inlet velocity boundary conditions are hard to obtain and that constant pressure inlet boundary conditions are feasible alternatives. A one-dimensional model is presented which can serve as a computationally inexpensive replacement of the three-dimensional brain model to ease parameter optimisation, sensitivity analyses and uncertainty quantification.

The findings of the present study can be generalised to organ-scale porous perfusion models. The results increase the applicability of computational tools regarding treatment development for stroke and other cerebrovascular conditions.

*Corresponding author: Tamás István Józsa, tamas.jozsa@eng.ox.ac.uk

bioRxiv preprint doi: https://doi.org/10.1101/2021.02.18.431511; this version posted February 18, 2021. The copyright holder for this preprint (which was not certified by peer review) is the author/funder, who has granted bioRxiv a license to display the preprint in perpetuity. It is made available under aCC-BY 4.0 International license.

1 Introduction

Cerebrovascular diseases including stroke impose a heavy burden on society [1]. The majority of stroke cases are caused by a thrombus blocking a major cerebral artery leading to severe blood shortage in the brain (ischaemic stroke). In recent decades, ischaemic stroke treatment has been revolutionised by thrombolysis (dissolving of blood clot with a thrombolytic agent) [2] and thrombectomy (mechanical thrombus removal with a stent retriever) [3, 4]. Advancing the related clinical procedures has great potential to benefit stroke patients but is tied entirely to resource intensive animal experiments and clinical trials [3–7]. To ease this task, the *In Silico* clinical trials for the treatment of acute Ischaemic STroke (INSIST) consortium aims to develop computational models of stroke and its treatments [8]. Once reliable models are available, *in silico* clinical trials could sharpen the focus of clinical trials and hence save time and money [9–11].

Estimating brain perfusion in both healthy and occluded scenarios is an important element of the INSIST pipeline and serves as a bridge between localised treatment effects and patient outcome [8]. To this end, a multi-scale haemodynamic model is under development which combines a one-dimensional (1D) network model of large arteries [12, 13] and a three-dimensional (3D) porous perfusion model [14] to simulate blood flow in the entire vasculature. The models will be coupled strongly through the cortical surface. The envisaged interface will facilitate communication between the boundary conditions of the models, namely pressure and volumetric flow rate values averaged over cortical territories [13]. Previously somewhat similar weak-coupling schemes have been established between a lumped parameter model and a porous continuum model to cover arteriole boundary conditions at the brain surface [15–19]. This approach preserves the two models as independent functional units and avoids the positioning of volumetric sources required for volumetric coupling [20–22]. The anatomical connection between large arteries and the microcirculation is crucial in ischaemic stroke modelling because it determines the location and extent of ischaemic regions. Another advantage of placing the interface at the cortical surface is that anatomical connections are preserved at the cortical surface so that subcortical vessels can be homogenised to lower computational costs. In the case of volumetric coupling, subcortical arterioles must be added to the one-dimensional network model to account for such connections which can drastically increase the number of discretised branches.

Computational porous and poroelastic models have been applied over a number of decades and have been proposed to describe aspects of cardiac [23–25] and cerebal biomechanics [15–19, 26]. Such organ-scale computational models have been applied to capture both healthy and pathophysiological states, such as brain injury [27–29], oedema [30], conditions associated with dementia [15, 18, 19], and ischaemic stroke [14]. The majority of these models utilise the Finite Element (FE) method [14–19, 27–30] with relatively few exceptions [20–22]. The present study focuses on a porous perfusion FE model developed specifically to capture blood flow changes in ischaemic stroke [14] as part of the *in silico* trial pipeline of INSIST [8]. Even though organ-scale porous and poroelastic brain models are becoming increasingly popular [14–19, 22, 26–32], efforts regarding their verification, validation [15], comprehensive sensitivity analysis [22, 33], and uncertainty quantification [31, 32] remain relatively rare and there is thus a need to fill this gap before the models are applied for clinical trial design and decision making.

Recently, the American Society of Mechanical Engineers (ASME) has introduced the Verification and Validation (V&V) 40 standard (titled "Assessing Credibility of Computational Modeling through Verification and Validation: Application to Medical Devices") [34], which details the requirements that a credible engineering software needs to satisfy to ensure safe applicability in the medical device industry. The present study thus sets out to establish guidelines regarding the efficient usage of a porous cerebral perfusion Finite Element model [14]

bioRxiv preprint doi: https://doi.org/10.1101/2021.02.18.431511; this version posted February 18, 2021. The copyright holder for this preprint (which was not certified by peer review) is the author/funder, who has granted bioRxiv a license to display the preprint in perpetuity. It is made available under aCC-BY 4.0 International license.

both in terms of accuracy and computational cost. To this end, simulations will be compared to exact analytical solutions and a thorough sensitivity analysis will be carried out covering every numerical and physiological model parameter. The results prepare the ground for uncertainty quantification, virtual patient generation, and validation, which are essential to carry out reliable *in silico* trials of ischaemic stroke treatments.

2 Methodology

Inspired by recent advances in the fields of heart [23–25] and brain [15–19] haemodynamic modelling, a multi-compartment porous continuum framework is utilised to describe time-averaged cerebral blood flow in the microcirculation embedded within brain tissue. The general partial differential equation set describing a steady-state multi-compartment Darcy system [15–19, 23–25] is written in a compact form[1] as

$$\nabla \cdot (\boldsymbol{K}_i \nabla p_i) = \sum_{j=1}^{n} \beta_{i,j}(p_i - p_j) - S_i. \tag{1}$$

Here, p_i denotes the Darcy pressure in the ith compartment and $\boldsymbol{K}_i$ is the corresponding permability symbolising flow conductance through pores with well-separated length scales. Considering n compartments, $i = 1,\ 2, \ldots\ n$ and $\beta_{i,j}$ is the intercompartment coupling coefficient matrix with $n \times n$ elements representing conductance between compartments i and j. It follows that $\beta_{i,j} = 0$ if $i = j$. A volumetric source term in the ith compartment is defined by S_i.

Considering a domain of interest denoted by Ω with a boundary $\partial\Omega = \Gamma = \Gamma_{D,i} \cup \Gamma_{N,i}$, a set of Dirichlet type boundary conditions (DBC) and Neumann type boundary conditions (NBC) are formulated as

$$p_i = a_i \quad \text{on } \Gamma_{D,i}, \text{ and} \tag{2}$$

$$(\boldsymbol{K}_i \cdot \boldsymbol{\nabla} p_i) \cdot \boldsymbol{n} = b_i \quad \text{on } \Gamma_{N,i}. \tag{3}$$

Here, $\boldsymbol{n}$ is the outward-pointing unit vector perpendicular to the boundary surface. Thereafter, the weak form can be derived by multiplying every component of Eq. (1) with a non-zero test function t_i, integrating over Ω and applying the divergence theorem:

$$\int_\Omega (\boldsymbol{K}_i \cdot \boldsymbol{\nabla} p_i) \cdot (\boldsymbol{\nabla} t_i)\, \mathrm{d}\Omega = \int_\Omega S_i t_i \mathrm{d}\Omega + \int_{\Gamma_{N,i}} b_i t_i \mathrm{d}\Gamma_{N,i} - \sum_{j=1}^{N} \int_\Omega \beta_{i,j}(p_i - p_j) t_i \mathrm{d}\Omega. \tag{4}$$

Eq. (4) is discretised by the continuous Bubnov-Galerkin method [35]. Numerical solutions of p_i are obtained with the open source FEniCS library [36–38] using first or second order Lagrange elements denoted by P_1 and P_2, respectively. The permeability tensors $\boldsymbol{K}_i$ and the coupling coefficients $\beta_{i,j}$ are captured by piecewise constant, zeroth order discontinuous elements (dP_0) unless stated otherwise. For simplicity, we restrict ourselves to a model with arteriole ($i = 1 = a$), capillary ($i = 2 = c$), and venule ($i = 3 = v$) compartments, and then generalise our findings whenever it is possible.

Numerical solutions of linear equation systems originating from the FE discretisation are obtained iteratively based on the BiCojungate Gradient STABilised method (BiCGSTAB) [39]. Computations are accelerated with an Algebraic MultiGrid (AMG) preconditioner [40]. Simulations were run on a desktop with an Intel Xeon E-2146G processor and 32 GB RAM unless

[1] Einstein summation convention is not utilised in this study.

bioRxiv preprint doi: https://doi.org/10.1101/2021.02.18.431511; this version posted February 18, 2021. The copyright holder for this preprint (which was not certified by peer review) is the author/funder, who has granted bioRxiv a license to display the preprint in perpetuity. It is made available under aCC-BY 4.0 International license.

stated otherwise. In order to verify the resulting model and carry out a comprehensive sensitivity analysis, three test cases are considered as detailed in the following subsections.

2.1 Three-dimensional synthetic data

To derive manufactured solutions [41], we assume solution functions of Eq. (1) of the form

$$p_1^{\mathrm{MS}} = (16x^2 - 32x^3 + 16x^4)(16y^2 - 32y^3 + 16y^4)z^2; \tag{5a}$$
$$p_2^{\mathrm{MS}} = (16x^2 - 32x^3 + 16x^4)(16y^2 - 32y^3 + 16y^4)(16z^2 - 32z^3 + 16z^4); \tag{5b}$$
$$p_3^{\mathrm{MS}} = -(16x^2 - 32x^3 + 16x^4)(16y^2 - 32y^3 + 16y^4)z^2. \tag{5c}$$

Polynomial functions are chosen to ensure straightforward differentiation of the pressure terms in Eq. (1). The permeability tensors are set to

$$\boldsymbol{K}_1 = \begin{bmatrix} 0 & 0 & 0 \\ 0 & 0 & 0 \\ 0 & 0 & 0.1(2-z) \end{bmatrix}, \quad \boldsymbol{K}_2 = \begin{bmatrix} 0.1 & 0 & 0 \\ 0 & 0.1 & 0 \\ 0 & 0 & 0.1 \end{bmatrix}, \quad \text{and} \quad \boldsymbol{K}_3 = \begin{bmatrix} 0 & 0 & 0 \\ 0 & 0 & 0 \\ 0 & 0 & 0.2(2-z) \end{bmatrix}, \tag{6}$$

whereas the non-zero elements of the coupling coefficient matrix are

$$\beta_{1,2} = \beta_{2,1} = 1.5 + 0.5\tanh(10z - 5), \quad \text{and} \tag{7a}$$
$$\beta_{2,3} = \beta_{3,2} = 3 + \tanh(10z - 5). \tag{7b}$$

The source terms S_1, S_2 and S_3 satisfying Eq. (1) can be obtained simply by substituting Eqs. (5c)-(7b) into Eq. (1). The source terms are set to zero in every other test case (details in Sections 2.3 and 2.2). $\boldsymbol{K}_i$ and $\beta_{i,j}$ are approximated by fourth order polynomials for the finite element computations.

The domain of interest chosen here is a unit cube $\Omega = [0,\ 1] \times [0,\ 1] \times [0,\ 1]$ with periodic boundary conditions applied on four sides:

$$p_i(0, y, z) = p_i(1, y, z), \text{ and} \tag{8}$$
$$p_i(x, 0, z) = p_i(x, 1, z). \tag{9}$$

Eqs. (8) and (9) define four DBCs in every compartment and another one is added in the arteriole ($i = 1$) and the venule ($i = 3$) compartments based on the manufactured solutions such that

$$p_i(x, y, 1) = p_i^{\mathrm{MS}}(x, y, 1). \tag{10}$$

Thereafter, the equation set is closed by prescribing homogeneous NBCs on the remaining surfaces (in Eq. (3) $b_i = 0$).

2.2 Three-dimensional human brain

Details of the baseline human brain simulation are provided in [14] and therefore only the most important settings are covered here. The computational domain (Ω) is obtained by postprocessing a tetrahedral patient-specific head model utilised in multiple recent studies [14, 42–44]. The geometry depicted in Fig. 1a is remeshed with tetrahedral elements using Tetgen [45]. The volumetric region of interest includes both grey matter (Ω_G) and white matter (Ω_W) subdomains, so that $\Omega = \Omega_G \cup \Omega_W$ as depicted in Fig. 1b. The bounding surface regions ($\partial\Omega$) include a transverse cut-plane of the brainstem Γ_{BS}, the ventricles Γ_V and the pial surface Γ_P so that $\partial\Omega = \Gamma_{BS} \cup \Gamma_V \cup \Gamma_P$ as depicted in Figs. 1a and c. The boundary region associated with the pial surface (Fig. 1a) is subdivided into eight perfusion territories corresponding to

bioRxiv preprint doi: https://doi.org/10.1101/2021.02.18.431511; this version posted February 18, 2021. The copyright holder for this preprint (which was not certified by peer review) is the author/funder, who has granted bioRxiv a license to display the preprint in perpetuity. It is made available under aCC-BY 4.0 International license.

major feeding arteries as shown in Figs. 1d-f. Perfusion territories have been identified using a voxelised atlas created based on vessel-encoded arterial spin labelling (ASL) perfusion magnetic resonance imaging (MRI) [46–50]. Then, the surface region that is perfused, for instance, by the Right Middle Cerebral Artery (R-MCA) is denoted by $\Gamma_{\text{R-MCA}}$. This approach ensures that blood arrives to the domain through cortical surface regions mirroring anatomical connections between large arteries and the microcirculation as shown in Figs. 1d-f.

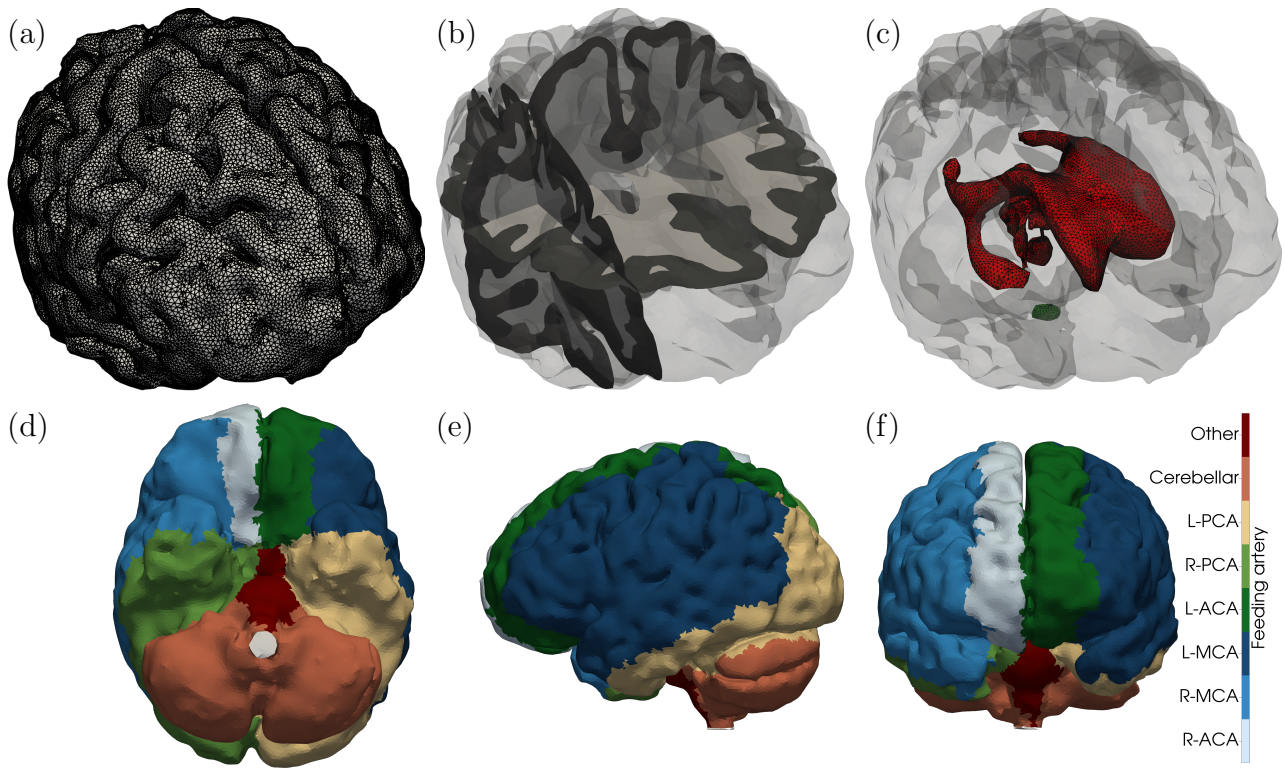

Figure 1: Human brain model: (a) pial surface; (b) grey and white matter visualised along coronal, sagittal and transverse planes; (c) ventricles (red) and cut-plane at brainstem (green); transverse (d), sagittal (e), and coronal (f) views of superficial perfusion territories. Reproduced with permission from Józsa *et al.* [14].

The imposed baseline boundary conditions prescribe zero flow through the transverse cut-plane of the brainstem and the surface of the ventricles:

$$\boldsymbol{K_i} \nabla p_i \cdot \boldsymbol{n} = 0 \quad \text{on } \Gamma_{BS} \text{ and } \Gamma_V. \tag{11}$$

Flow through the pial surface in the capillary compartment is zero:

$$\boldsymbol{K_c} \nabla p_c \cdot \boldsymbol{n} = 0 \quad \text{on } \Gamma_P. \tag{12}$$

Because of the incompressible fluid flow model, the results depend solely on the cerebral perfusion pressure (CPP) defined as the arteriole-venule pressure difference at the pial surface: $\text{CPP} = p_a - p_v$. Setting the zero level of the pressure at the outlet of the venous compartment (p_v) leads to

$$p_a = \text{CPP} + p_v \quad \text{on } \Gamma_P. \tag{13}$$

Pressure values in the case of 3D brain simulations are presented relative to the venous outlet pressure p_v. To account for totally occluded scenarios, blood flow through the perfusion territory of an occluded vessel is set to zero whereas surface pressure is assumed to remain constant in other regions. Accordingly, a R-MCA occlusion is modelled with zero flux through

bioRxiv preprint doi: https://doi.org/10.1101/2021.02.18.431511; this version posted February 18, 2021. The copyright holder for this preprint (which was not certified by peer review) is the author/funder, who has granted bioRxiv a license to display the preprint in perpetuity. It is made available under aCC-BY 4.0 International license.

the corresponding cortical territory ($\Gamma_{\text{R-MCA}}$) so that the resulting mixed boundary conditions become

$$\frac{\partial p_a}{\partial \boldsymbol{n}} = 0 \quad \text{on } \Gamma_{\text{R-MCA}}, \text{ and} \tag{14a}$$

$$p_a = \text{CPP} + p_v \quad \text{on } \Gamma_P \setminus \Gamma_{\text{R-MCA}}. \tag{14b}$$

The model is parametrised based on several simplifications as discussed in [14]. Considering that the arteriole-capillary ($\beta^G_{1,2} = \beta^G_{2,1}$) and capillary-venule ($\beta^G_{2,3} = \beta^G_{3,2}$) coupling coefficients are known in the grey matter, it is assumed that the ratio of grey and white matter coupling coefficients (β^G/β^W) is constant. It has been demonstrated based on microscale one-dimensional haemodynamic network simulations that the capillary permeability tensor is isotropic and characterised by a scalar k_2 [51]. It is hypothesised that a reference coordinate system [ξ, η, ζ] can be found at every point so that ζ is parallel to the local axis of the descending arterioles and ascending venules. In this coordinate system, the anisotropic arteriole ($\boldsymbol{K}_1^{\text{ref}}$) and venule ($\boldsymbol{K}_3^{\text{ref}}$) permeability tensors are modelled as tensors with a single non-zero diagonal element (k_1 and k_3) because they represent vessel bundles:

$$\boldsymbol{K}_1^{\text{ref}} = \begin{bmatrix} 0 & 0 & 0 \\ 0 & 0 & 0 \\ 0 & 0 & k_1 \end{bmatrix}, \quad \text{and} \quad \boldsymbol{K}_3^{\text{ref}} = \begin{bmatrix} 0 & 0 & 0 \\ 0 & 0 & 0 \\ 0 & 0 & k_3 \end{bmatrix}. \tag{15}$$

The [ξ, η, ζ] coordinate system is determined assuming that penetrating vessels grow from the pial surface to the ventricles following a vector field. This vector field is computed as a gradient of a scalar field governed by a single diffusion equation [14]. It is worth noting that no other methods have been proposed to obtain these anisotropic permeability fields even though they play a crucial role in predicting perfusion response to vessel occlusion.

2.3 One-dimensional brain tissue column

Eq. (1) can be simplified so that a one-dimensional problem with homogeneous permeabilities can be posed and defined by a set of ordinary differential equations in the form of

$$k_i \frac{\mathrm{d}^2 p_i}{\mathrm{d}x^2} = \sum_{j=1}^{n} \beta_{i,j}(p_i - p_j). \tag{16}$$

Here, the permeability of each compartment (k_i) is a scalar. Introducing the dimensionless variables $x^* = x/l_s$ and $p^* = p/p_s$ based on a length scale (l_s) and a pressure scale (p_s) leads to a dimensionless form of Eq. (16) as

$$\frac{\mathrm{d}^2 p_i^*}{\mathrm{d}x^{*2}} = \sum_{j=1}^{n} \alpha_{i,j}^*(p_i^* - p_j^*). \tag{17}$$

The dimensionless matrix group $\alpha_{i,j}^* = l_s^2 \beta_{i,j}/k_i$ provides a similarity condition for Eq. (16).

Equation (17) describes n second order ordinary differential equations. This system can be replaced by $2n$ first order ordinary differential equations once the pressure gradient $q_i^* = \mathrm{d}p_i^*/\mathrm{d}x^*$ is introduced. Thereafter, the unknown vector

$$\boldsymbol{r}^* = [\boldsymbol{p}^*;\ \boldsymbol{q}^*] \tag{18}$$

contains the pressure p_i^* and pressure gradient q_i^* functions for each compartment. Finally, a matrix differential equation based on Equation (17) can be formulated as

$$\boldsymbol{r}^{*\prime} = \boldsymbol{A}\boldsymbol{r}. \tag{19}$$

bioRxiv preprint doi: https://doi.org/10.1101/2021.02.18.431511; this version posted February 18, 2021. The copyright holder for this preprint (which was not certified by peer review) is the author/funder, who has granted bioRxiv a license to display the preprint in perpetuity. It is made available under aCC-BY 4.0 International license.

Here, the prime ($'$) denotes spatial differentiation and the $\boldsymbol{A}$ matrix is

$$\boldsymbol{A} = \begin{bmatrix} \boldsymbol{0} & \boldsymbol{I} \\ \boldsymbol{B} & \boldsymbol{0} \end{bmatrix}, \tag{20}$$

where every submatrix has a dimension of $n \times n$, and $\boldsymbol{I}$ is the identity matrix. The connection between the coupling coefficient matrix $\boldsymbol{\alpha} = \alpha_{i,j}$ and the submatrix $\boldsymbol{B}$ is given by

$$\boldsymbol{B} = \mathrm{diag}(\boldsymbol{\alpha}\boldsymbol{e}_n) - \boldsymbol{\alpha}. \tag{21}$$

Here, the n dimensional vector $\boldsymbol{e}_n$ is filled with ones, and the "diag" operator is used to turn a column vector into a diagonal square matrix.

The solution of Equation (19) is

$$\boldsymbol{r} = \Re\left(\sum_{j=1}^{2n} C_j \boldsymbol{v_j} \mathrm{e}^{\lambda_j x}\right). \tag{22}$$

Here, λ_j and $\boldsymbol{v_j}$ are the jth eigenvalue and eigenvector of $\boldsymbol{A}$, respectively. $\Re$ is used to take the real part of the expression and to handle complex eigenvalue and eigenvector pairs.

The C_j coefficients are determined based on combinations of DBCs and NBCs at x_b. A DBC in compartment i reads as

$$p_i^*(x^* = x_b^*) = a_i^*. \tag{23}$$

Based on the unknown vector defined in Eq. (18) and the solution expression Eq. (22), a DBC can be satisfied by imposing

$$r_i^*(x^* = x_b^*) = p_i^*(x^* = x_b^*) = \Re\left(\sum_{j=1}^{2n} C_j v_j^i \mathrm{e}^{\lambda_j x_b}\right) = a_i^*. \tag{24}$$

Here, $r_i = p_i^*$ denotes the ith element of $\boldsymbol{r}$ and v_j^i is the ith element of jth eigenvector. A NBC in compartment i is defined as

$$\left.\frac{\mathrm{d}p_i^*}{\mathrm{d}x^*}\right|_{x^*=x_b} = b_i^*, \tag{25}$$

The second half of the unknown vector defined in Eq. (18) includes the pressure gradients. Therefore, a NBC can be satisfied by imposing

$$r_{i+n}^*(x^* = x_b^*) = q_i^*(x^* = x_b^*) = \Re\left(\sum_{j=1}^{2n} C_j v_j^{i+n} \mathrm{e}^{\lambda_j x_b}\right) = b_i^*. \tag{26}$$

Eqs. (24) and (26) provide a single equation for each boundary condition. Considering n compartments, the $2n$ boundary conditions lead to $2n$ linear equations based on the $2n$ coefficients of the solution expressions (C_j). The resulting linear equation system determines uniquely the coefficients of the solution expressions (C_j). Using the DBC (23) and the NBC (25), the procedure can be extended to handle multiple subdomains with different coupling coefficients. In such cases, interface conditions have to be applied to ensures that the solution is continuously differentiable. Therefore, this analytical method is suitable to obtain solutions for a column of brain tissue stretching between the cortical and ventricular surfaces. The method can handle a domain including grey and white matter with identical permeabilities but different coupling coefficient matrices.

bioRxiv preprint doi: https://doi.org/10.1101/2021.02.18.431511; this version posted February 18, 2021. The copyright holder for this preprint (which was not certified by peer review) is the author/funder, who has granted bioRxiv a license to display the preprint in perpetuity. It is made available under aCC-BY 4.0 International license.

3 Results and Discussion

3.1 Spatial resolution

3.1.1 Manufactured solutions

The suitability of the finite element method is evaluated based on the manufactured solution shown in Fig. 2. A uniform tetrahedral mesh is generated with two elements along each edge of the cube and uniformly refined four times. Then, a grid convergence study is carried out using first (P_1) and second order (P_2) elements as summarised in Table 1. The analytical solution and the finite element approximation along the sampling line depicted in Fig. 2 are shown in Fig. 3a, highlighting that a very good agreement is achievable. Fig. 3b presents the L_2-norm defined over the entire domain based on the difference between the analytical and the numerical solutions. With increasing spatial resolution, the L_2-norm decreases as expected. Superconvergence of the solution with first order elements can be observed which is a well-known feature of this FE approximation [52].

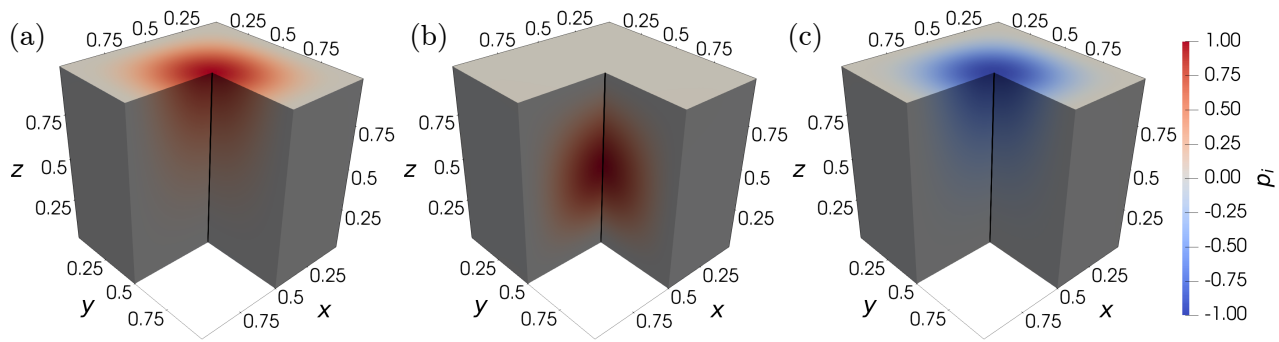

Figure 2: Manufactured solution in a unit cube visualised in the arteriole $i = 1$ (a), capillary $i = 2$ (b), and venule $i = 3$ (c) compartments with a sampling line $(0.5,\ 0.5\ , z)$.

NGS	n_{edge}	n_{volume}	Element order	L_2-norm	$\partial p_1/\partial z$ at $(0.5, 0.5, 1)$	t_{inv} [s]
16	2	48	1	0.15174	1.273	0.0042
8	4	384	1	0.08714	1.800	0.0287
4	8	3072	1	0.02857	1.867	0.2278
2	16	24576	1	0.00771	1.927	1.8428
1	32	196608	1	0.00197	1.965	15.0789
16	2	48	2	0.06215	1.824	0.0161
8	4	384	2	0.01399	2.006	0.1403
4	8	3072	2	0.00266	2.008	1.4050
2	16	24576	2	0.00060	1.999	16.3241
1	32	196608	2	0.00014	1.998	162.1361

Table 1: Results corresponding to the grid convergence study using manufactured solutions. Normalised Grid Spacing (NGS), number of elements along each edge of the unit cube (n_{edge}); total number of elements (n_{volume}); wall time required for the iterative solution of the linear system (t_{inv}).

According to Fig. 3b and Table 1, solutions achieved using a second order scheme on a given mesh have about the same L_2-norm as first order approximations after a single refinement. However, it is important to emphasise that the convergence of pointwise variables does not

bioRxiv preprint doi: https://doi.org/10.1101/2021.02.18.431511; this version posted February 18, 2021. The copyright holder for this preprint (which was not certified by peer review) is the author/funder, who has granted bioRxiv a license to display the preprint in perpetuity. It is made available under aCC-BY 4.0 International license.

necessarily follow the convergence trend of integral quantities. Fig. 3c suggests that the second order FE scheme outperforms the first order scheme in terms of gradient estimation even if computations with the latter are carried out with a threefold refined mesh. Beyond accuracy, the computational cost of simulations as a function of the spatial resolution and the element order can be examined in Fig. 3d. In general, computations with second order elements take one order of magnitude longer and are comparable to the computational cost of simulations with first order elements on a refined mesh (see also Table 1).

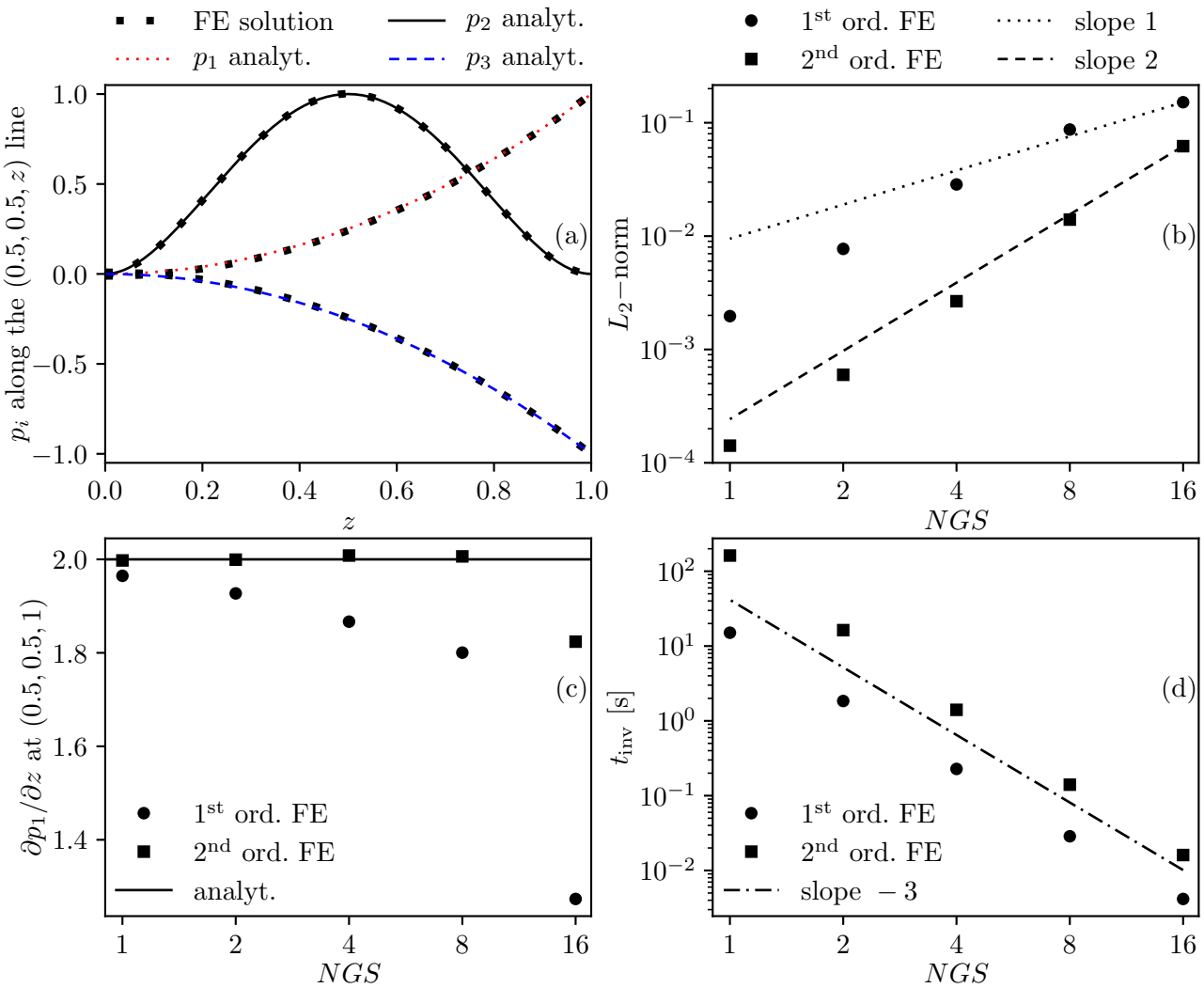

Figure 3: Exact manufactured solutions and FE approximations with second order (ord.) elements and normalised grid spacing (NGS) 2 along a line (a). Numerical error of the FE approximation (b), FE approximation and exact value of the arteriole gradient at a single point (c), and wall time of the linear system matrix inversion (t_{inv}) (d) as functions of the NGS and element order.

3.1.2 Whole brain model

Next, simulations are carried out with the whole brain model to investigate how uncertainty of the gradient estimation near the boundaries impacts the results. Two scenarios are considered using previously optimised settings [14] summarised in Table 2: baseline (healthy) and an RMCA occlusion. The algorithm used for parameter optimisation is described in Appendix A. In a porous framework, the pressure gradient is directly connected to the Darcy velocity vector

bioRxiv preprint doi: https://doi.org/10.1101/2021.02.18.431511; this version posted February 18, 2021. The copyright holder for this preprint (which was not certified by peer review) is the author/funder, who has granted bioRxiv a license to display the preprint in perpetuity. It is made available under aCC-BY 4.0 International license.

which can be introduced in compartment i as

$$\boldsymbol{u}_i = -\boldsymbol{K}_i \nabla p_i. \tag{27}$$

From here, the overall volumetric flow rate entering the arteriole compartment through the pial surface Γ_P is simply defined as

$$Q^\Gamma = -\int_\Gamma \boldsymbol{u}_1 \mathrm{d}(\Gamma \boldsymbol{n}) = \int_\Gamma \boldsymbol{K}_1 \nabla p_1 \mathrm{d}(\Gamma \boldsymbol{n}), \tag{28}$$

The $\Gamma \boldsymbol{n}$ product corresponds to an outward-pointing vector with magnitude equal to the area of the Γ boundary surface. (The Darcy velocity has non-zero components perpendicularly to the boundary surface only at Γ_P and therefore in Eq. (28) the integration domain Γ_P is replaced with Γ for a more concise notation.)

Parameter	Value	Reference	Unit	Optimised
k_1	1.234	4 [22]; 0.021 ± 0.019 [53]	$\mathrm{mm}^3\ \mathrm{s}\ \mathrm{kg}^{-1}$	Yes
$\beta^G_{i,j}/\beta^W_{i,j}$	2.538	1.6 [22]; 1.0 [15, 16, 18]	—	Yes
k_2	$4.28 \cdot 10^{-4}$	$4.28 \cdot 10^{-4}$ [51];	$\mathrm{mm}^3\ \mathrm{s}\ \mathrm{kg}^{-1}$	No
k_3/k_1	2	2 [22]	$\mathrm{mm}^3\ \mathrm{s}\ \mathrm{kg}^{-1}$	No
$\beta^G_{1,2}$	$1.326 \cdot 10^{-6}$	$1.5 \cdot 10^{-19}$ [15, 18]; $1.5 \cdot 10^{-7}$ [16] $5 \cdot 10^{-6}$ [22]; $(4.13 \pm 5.49) \cdot 10^{-5}$ [53]	$\mathrm{Pa}^{-1}\mathrm{s}^{-1}$	No
$\beta^G_{2,3}$	$4.641 \cdot 10^{-6}$	$1.5 \cdot 10^{-19}$ [15, 18]; $1.5 \cdot 10^{-7}$ [16] $5 \cdot 10^{-6}$ [22]	$\mathrm{Pa}^{-1}\mathrm{s}^{-1}$	No
CPP	75	78 ± 10 [54]	mmHg	—
$\beta^G_{1,2} + \beta^G_{2,3}$	$5.967 \cdot 10^{-6}$	10^{-5} [22];	$\mathrm{Pa}^{-1}\mathrm{s}^{-1}$	—

Table 2: List of model parameters and some reference values (mean $\pm$ standard deviation when available). The distribution of the parameters reported in [51] based on microscale vessel network simulations is not normal. The last column indicates which parameters are optimised as detailed in Appendix A.

Therefore, any uncertainty in the pressure gradient propagates directly to the volumetric flow rate. Accurate flow rate computation is important for two reasons: (i) superficial arteriole pressure and flow rates are cornerstones of a coupling scheme between the present continuum model and a network model of large arteries as detailed in Section 1; (ii) surface fluxes associated with major cerebral arteries can be directly compared with values obtained from phase-contrast MRI [55] for validation purposes.

The multi-compartment formulation offers an alternative method to compute volumetric flow rate through the brain. Introducing perfusion $F = \beta_{1,2}(p_1 - p_2)$, and integrating it over the brain volume Ω leads to

$$Q^\Omega = \int_\Omega \beta_{1,2}(p_1 - p_2)\mathrm{d}\Omega = \int_\Omega F \mathrm{d}\Omega. \tag{29}$$

According to mass conservation $Q^\Omega = Q^\Gamma$ so the imbalance between the two formulations is present because the FE method is not conservative by default, unlike the finite volume method [56]. Two strategies are employed to mitigate the associated error: (i) grid refinement; and (ii) increasing FE orders of both the pressure and the velocity. For P_1 and P_2 pressure elements, the natural velocity pair is dP_0 and dP_1 but higher order velocity approximations can be obtained

bioRxiv preprint doi: https://doi.org/10.1101/2021.02.18.431511; this version posted February 18, 2021. The copyright holder for this preprint (which was not certified by peer review) is the author/funder, who has granted bioRxiv a license to display the preprint in perpetuity. It is made available under aCC-BY 4.0 International license.

by projection. The results in Table 3 summarise the tested cases and show that the volumetric flow rate from Eq. (29) depends on the grid size and the element order only negligibly. The error in Q^{Ω} should be relatively low in the investigated cases because the computed values overlap independently from the spatial resolution. For this reason, and because of the mass conservation principle, the relative difference,

$$\Delta_r Q^{\Gamma} = \frac{Q^{\Gamma} - Q^{\mathrm{ref}}}{Q^{\mathrm{ref}}} \cdot 100\% = \frac{Q^{\Gamma} - Q^{\Omega}}{Q^{\Omega}} \cdot 100\%, \tag{30}$$

is used for error measurement.

Figs. 4a and b show the imbalance between Q^{Ω} and Q^{Γ} highlighting that without improved $\boldsymbol{u}_i$ approximation the surface flux is always underestimated by Q^{Γ}. Both refinement and increased FE order can mitigate the error of Q^{Γ}. However, higher order pressure and velocity approximations are required to keep $|\Delta_r Q^{\Gamma}| < 5\%$. Fig. 4c displays the wall time of the simulations emphasising the increased computational cost required for more accurate flux estimations. In summary, second order velocity and pressure elements on a relatively coarse mesh (about 10^6 elements) can provide a reasonable compromise between accuracy and performance if computing Q^{Γ} is important. Otherwise, perfusion and pressure distributions can be estimated reasonably well on coarse meshes with about 1 million elements.

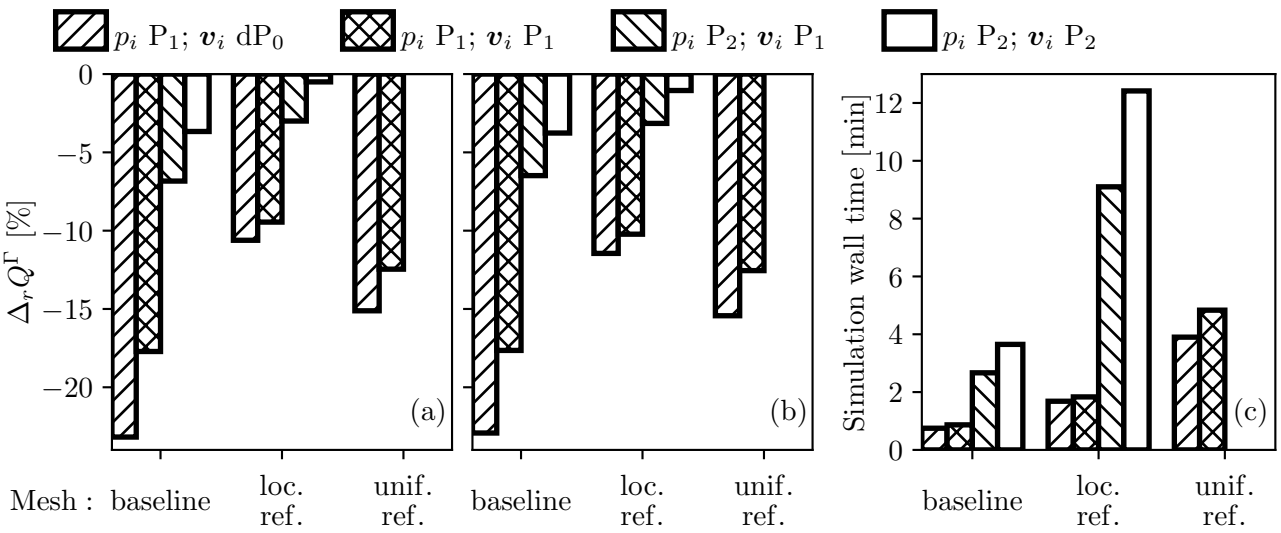

Figure 4: Relative error of the superficial volumetric flow rate estimation as functions of the spatial resolution and the FE order in the case of the baseline (a) and RMCA occlusion (b) scenarios. Computational time averaged between the healthy and the occluded cases (c). The "loc. ref." and "unif. ref." abbreviations correspond to locally and uniformly refined meshes, respectively (see Tab. 3 for further details).

Once it is established under what conditions the present 3D model can provide accurate estimation of volumetric flow rate through cortical surface regions, it is possible to compute volumetric flow rate of the major cerebral arteries. Simulation results are compared with values from a clinical study in Tab. 4. Whereas the model is optimised for overall brain perfusion, blood flow rate through these major arteries provide a chance for independent validation. It is promising that volumetric flow rate in both the ACA and the MCA is predicted within one standard deviation of the experimental values. Volumetric flow rate in the PCA is somewhat overestimated. This simple comparison is an important milestone in the quantitative validation of the 3D brain model and provides guidance about development directions for the future.

The results emphasise the importance of accurate mapping between voxelised vascular atlases and the triangulated brain surface and draw attention to geometrical flaws. The brain

bioRxiv preprint doi: https://doi.org/10.1101/2021.02.18.431511; this version posted February 18, 2021. The copyright holder for this preprint (which was not certified by peer review) is the author/funder, who has granted bioRxiv a license to display the preprint in perpetuity. It is made available under aCC-BY 4.0 International license.

model does not capture the lateral sulcus and the insula. Because of these neglected regions, the brain surface is underestimated whereas the brain volume is overestimated (see Tab. 4). It is anticipated that the 3D porous model will provide more reliable volumetric flow rate estimations once these geometrical issues are overcome. However, obtaining accurate discretised brain geometries suitable for FE computations remains a challenging task, partially because of labelling the boundary regions, and therefore such efforts are left to a future study.

				healthy		RMCA occl.	
Mesh	n_{vol}	p_i FE	$\boldsymbol{v}_i$ FE	Q^{Ω}	Q^{Γ}	Q^{Ω}	Q^{Γ}
baseline	1,042,301	P_1	dP_0	604	464	493	380
		P_1	P_1	604	497	493	406
		$P_2^{\star}$	$P_1^{\star}$	600*	559*	478*	447*
		P_2	P_2	600	578	478	460
loc. ref.	3,400,570	P_1	dP_0	603	539	489	433
		P_1	P_1	603	546	489	439
		P_2	P_1	600	582	476	461
		$\boldsymbol{P_2}$	$\boldsymbol{P_2}$	**600**	**597**	**476**	**471**
unif. ref.	8,338,408	P_1	dP_0	602	511	486	411
		P_1	P_1	602	527	486	425

Table 3: Results corresponding to the grid sensitivity analysis of the brain simulations. Due to the computational cost associated with the locally refined (loc. ref.) and the uniformly refined (unif. ref.) meshes, these simulations are run using 12 threads of an Intel Xeon E5-2640 processor and 128 GB RAM. Computations on the unif. ref. mesh with P_2 elements require more than 128 GB RAM and therefore they are omitted. * highlights the case used to evaluate the impact of pressure and velocity inlet BCs, whereas the bold text indicates the case with the smallest difference between Q^{Γ} and Q^{Ω}.

3.2 Boundary conditions

Results from the previous section draw attention to issues related to flux computation in a porous FE framework. Instead of constant pressure, uniform velocity has been used as an inlet BC [15–19], where the velocity is calculated as the ratio of a given volumetric flow rate and the inlet surface area. This NBC at the inlet might distort the results because of errors related to gradient estimation so we next investigate the difference between pressure and velocity inlets using the present model. To this end, a single simulation with constant inlet velocity is run with the same settings as the case in Tab. 3 marked with *.

The overall volumetric flow rate $Q^{\Omega} = 600$ [ml/min], and hence brain perfusion, is insensitive to the inlet boundary conditions. Q^{Γ} is impacted only slightly: pressure inlet leads to 559 [ml/min] whereas velocity inlet results in 572 [ml/min] (both values should be 600 [ml/min] based on mass conservation). The effects of the inlet boundary condition on other statistics regarding the pressure and the perfusion fields are shown in Fig. 5. Most of the volume averaged pressure ($\langle p_i \rangle$) and perfusion ($\langle p_i \rangle$) values are altered only slightly by the inlet boundary conditions. However, extrema of both the pressure and the perfusion fields change substantially when the inlet velocity BC is used. Minimum values are underestimated so that the relative difference of the minimum arteriole pressure and perfusion values are approximately -100% because min p_1 and min F) are close to zero when uniform inlet velocity BCs are used. By comparison, the inlet velocity BCs lead to overshot maximum values nearly by a factor of 10

bioRxiv preprint doi: https://doi.org/10.1101/2021.02.18.431511; this version posted February 18, 2021. The copyright holder for this preprint (which was not certified by peer review) is the author/funder, who has granted bioRxiv a license to display the preprint in perpetuity. It is made available under aCC-BY 4.0 International license.

compared to the case with inlet pressure BCs (see max p_1 and max F in Fig. 5).

In Figs. 6a-d, and b-e, the pressure and perfusion fields corresponding to inlet pressure and velocity BCs, respectively, emphasise further the difference between the two solutions. The arteriole velocity magnitude displayed over the cortical surface (Fig. 6c) shows that in the case of pressure inlet BC the velocity is strongly inhomogeneous. It is a remarkable feature of this scenario that high velocity values are predicted along the major cerebral arteries branching from the circle of Willis because the whole brain model does not include any information about the location of these vessels. The solution obtained with constant pressure BC suggests that descending arterioles branching from the major cerebral arteries play a key role in providing well-balanced grey and white matter perfusion. The velocity distribution over the cortical surface is not known *a priori* and therefore it is challenging to impose feasible velocity distributions with velocity inlet BC.

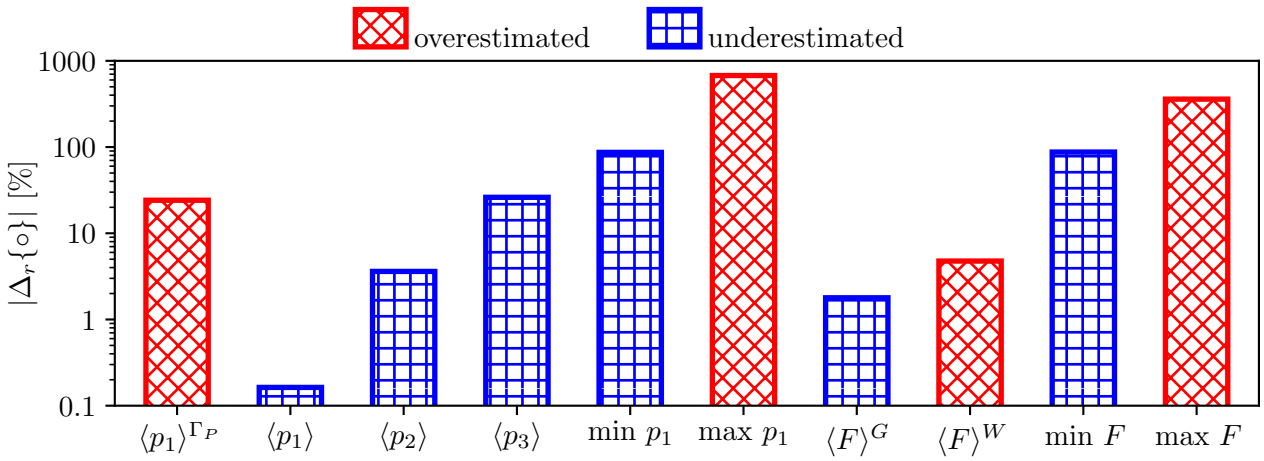

Figure 5: Absolute value of the relative difference between some statistics extracted from simulations carried out with inlet pressure and velocity BCs. Average arteriole pressure over the pial surface $\langle p_1\rangle^{\Gamma_P}$; average pressure in the arteriole ($\langle p_1\rangle$), capillary ($\langle p_2\rangle$), and venule ($\langle p_3\rangle$) compertments over the entire brain; minimum (min) and maximum (max) arteriole pressure (p_1) and perfusion (F); average perfusion in grey ($\langle F\rangle^G$) and white ($\langle F\rangle^W$) matter. The colour and pattern of each bar indicates whether results with the inlet velocity BCs overshoot or underestimate the reference values corresponding to the pressure inlet BCs.

	Simulation	Reference
Q ACA/MCA/PCA [ml/min]	66 / 126 / 67	75 ± 15 / 131 ± 23 / 51 ± 10 [55]
Q total [ml/min]	600	657 ± 94 [55]; 484 ± 88 [57]
A_{cortical} [cm^2]	1005	1770 [58]
V_b [ml]	1390	869 ± 99 [59]

Table 4: Comparison of some model parameters and results with literature data: volumetric flow rates of the anterior (ACA), middle (MCA) and posterior (PCA) cerebral arteries obtained by surface integration of the velocity vector over perfusion territories; cortical surface area (A_{cortical}) and brain volume (V_b).

The volumetric flow rates corresponing to boundary regions of the major cerebral arteries are summarised in Tab. 4. Based on previous clinical investigations [55, 57], it is clear that each major cerebral artery contributes differently to volumetric blood flow rate to the brain. Even if we assume that superficial perfusion territories of cerebral arteries are proportional to the

bioRxiv preprint doi: https://doi.org/10.1101/2021.02.18.431511; this version posted February 18, 2021. The copyright holder for this preprint (which was not certified by peer review) is the author/funder, who has granted bioRxiv a license to display the preprint in perpetuity. It is made available under aCC-BY 4.0 International license.

associated blood flow rate, it is important to recognise that the volumetric flow rate should be heterogeneous as dictated by underlying grey and white matter volumes. Although the validity of homogeneous inlet velocity is physiologically questionable, prescribing constant pressure inlets in healthy scenarios is supported indirectly by clinical data. Based on ASL MRI [47], cerebral perfusion regions have been found to be well-separated indicating that the pressure gradient between these territories is small. Furthermore, dynamic computed tomography angiograms indicate that flow through leptomeningeal collaterals is activated as a result of cerebral artery occlusion [60]. We hypothesise that in healthy cases, leptomeningeal collaterals [2, 50, 60–63] as well as pial arterioles [64–66] act to equalise blood pressure in descending arterioles near the cortical surface. This hypothesis could be tested once the present perfusion model and the 1D model incorporating the larger arteries [13] are coupled, and it is supported by pressure data obtained in rodents which suggest small pressure drop in large arteries compared to the microcirculation [67–69].

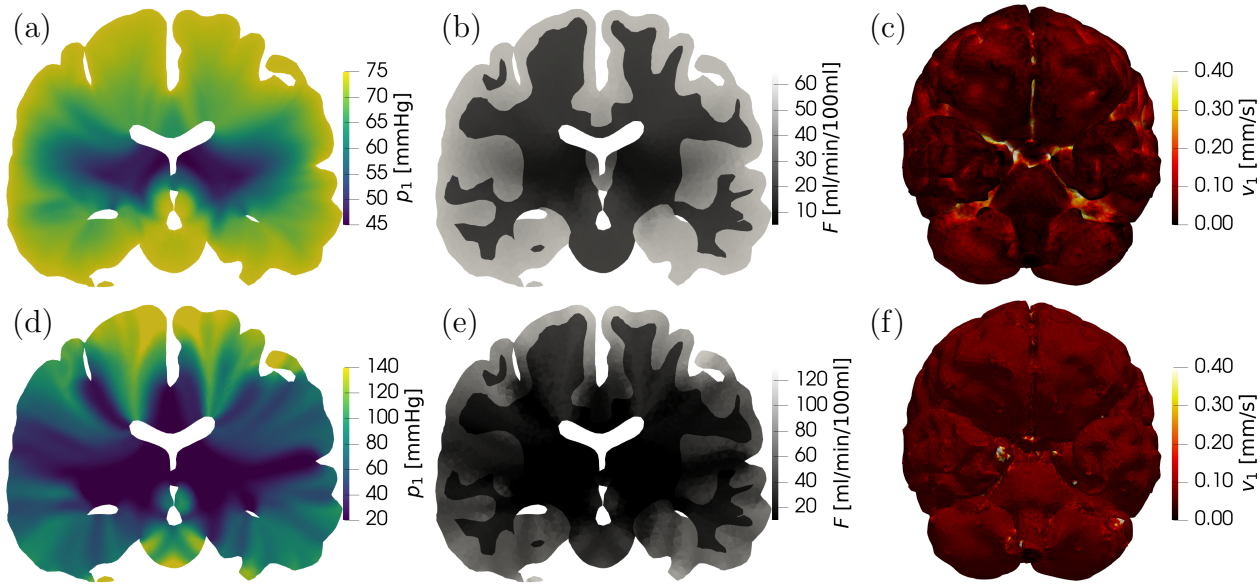

Figure 6: Pressure p_a (a-d) and perfusion F (b-e) distributions along a coronal plane, and velocity magnitude (c-f) along the cortical surface. Constant pressure inlet (a-c) and constant velocity inlet (d-f). In (f), the non-uniform velocity magnitude is associated with numerical errors. Results correspond to the mesh with local grid refinement at the boundaries and P_2 pressure and velocity elements (details in Table 3).

3.3 Sensitivity analysis

Determining the actual values of parameters in physiological models is a challenging task because of limited experimental data, high patient-specific variability, and the typically high dimensionality of the parameter spaces. Considering porous cerebral haemodynamics, this issue is far from being settled as indicated by the broad range of reported parameters summarised in Tab. 2. With increasing computational costs, mapping a high dimensional parameter space quickly becomes unfeasible. Beyond parameter optimisation, sensitivity analysis and the associated uncertainty quantification are other tasks which require large batches of simulations. Here we aim to utilise the one-dimensional model described in Section 2.3 in order to ease these tasks.

bioRxiv preprint doi: https://doi.org/10.1101/2021.02.18.431511; this version posted February 18, 2021. The copyright holder for this preprint (which was not certified by peer review) is the author/funder, who has granted bioRxiv a license to display the preprint in perpetuity. It is made available under aCC-BY 4.0 International license.

3.3.1 One-dimensional brain tissue column

The one-dimensional multi-compartment porous model enables the investigation of tissue columns including both grey and white matters so that the corresponding model parameters are identical with the ones used for the three-dimensional brain model (Tab. 2). In the 1D case, $x = 0$ and $x = l$ correspond to the pial and the ventricualar surfaces, respectively. Therefore, the same boundary conditions can be imposed in the 1D tissue column and the 3D brain. (Similarly to the 3D brain, pressure values in the 1D case are presented relative to the venous outlet pressure p_v.) Thereafter, the one-dimensional model has only two free parameters: the lengths of the grey (l_G) and the white (l_W) matter domains defined so that $l = l_G + l_W$. The equivalent $l_G = 13.55$ and $l_W = 7.99$ [mm] is uniquely determined by the human brain model used here and can be obtained by optimisation. The corresponding cost function is zero if the one-dimensional model returns $\langle F \rangle = 43$, $\langle F \rangle^G = 56$, and $\langle F \rangle^W = 21$ [ml/min/100ml] which overlap exactly with volume-averaged perfusion values of the three-dimensional brain model.

Fig. 7 displays the analytical pressure distributions in the arteriole, capillary and venule compartments. A one-dimensional FE approximation with 100 P_1 elements is also shown which is in excellent agreement with the analytical results. The average pressure values provided by the 1D model are within ±4% of those computed using the 3D brain in every case. One-dimensional simulations are approximately 3000 times faster compared to their 3D counterparts.

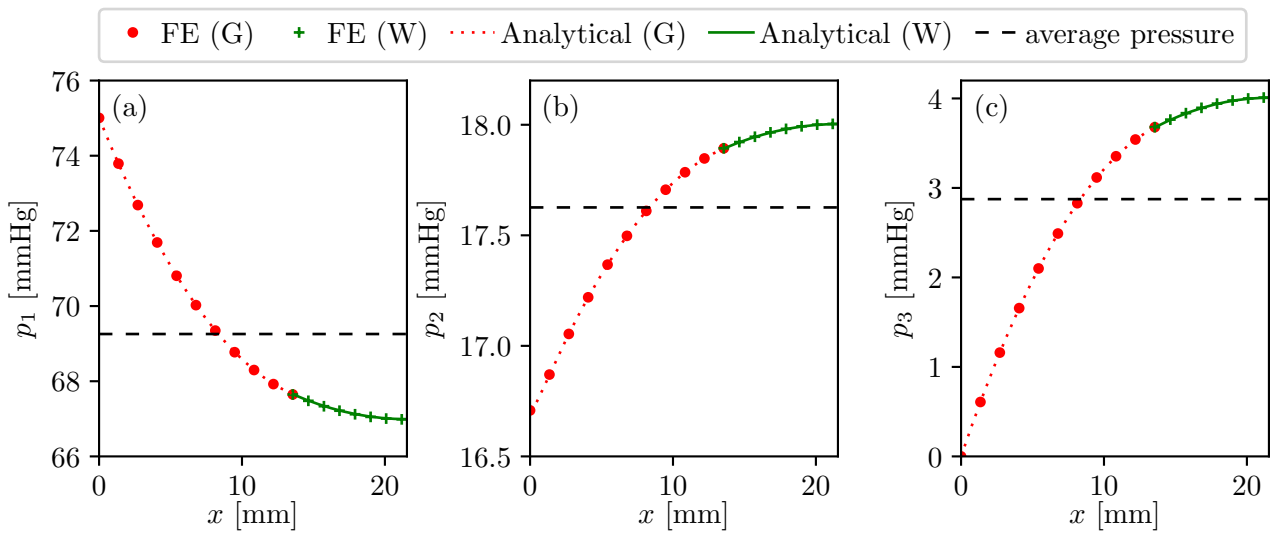

Figure 7: Analytical and numerical solutions of the one-dimensional problem representing a brain tissue column perpendicular to the cortical surface: arteriole (a), capillary (b) and venule (c) compartments. Results in both grey (G) and white (W) matter are displayed.

3.3.2 Mapping the parameter space

The 1D model is a good candidate for parameter space mapping because of its low computational cost. A disadvantage of the analytical formulation is that with the parameters presented in Tab. 2, the linear equation system governing the boundary conditions is very stiff probably because of the parameters with different . The condition number depends nonlinearly on the reference length scale used for the nondimensionalisation. To avoid the issue of suitable reference length scale selection, we will use the 1D finite element model verified in Fig. 7 for a detailed sensitivity analysis.

Next, each parameter is perturbed independently from others. The one-at-a-time approach is applicable and the corresponding sensitivity analysis is representative of the system behaviour becayse the governing equation set (1) is linear [33]. The parameter range is [10%;1000%] compared to the values in Tab. 2 with 101 samples along each dimension. In addition, a geometrical

bioRxiv preprint doi: https://doi.org/10.1101/2021.02.18.431511; this version posted February 18, 2021. The copyright holder for this preprint (which was not certified by peer review) is the author/funder, who has granted bioRxiv a license to display the preprint in perpetuity. It is made available under aCC-BY 4.0 International license.

scaling factor is introduced based on the ratio of the original and the perturbed volume of the computational domain. In order to evaluate whether the 1D model can capture the system behaviour, 11 samples along each dimension of the parameter space are tested with the 3D brain model using P_1 pressure elements.

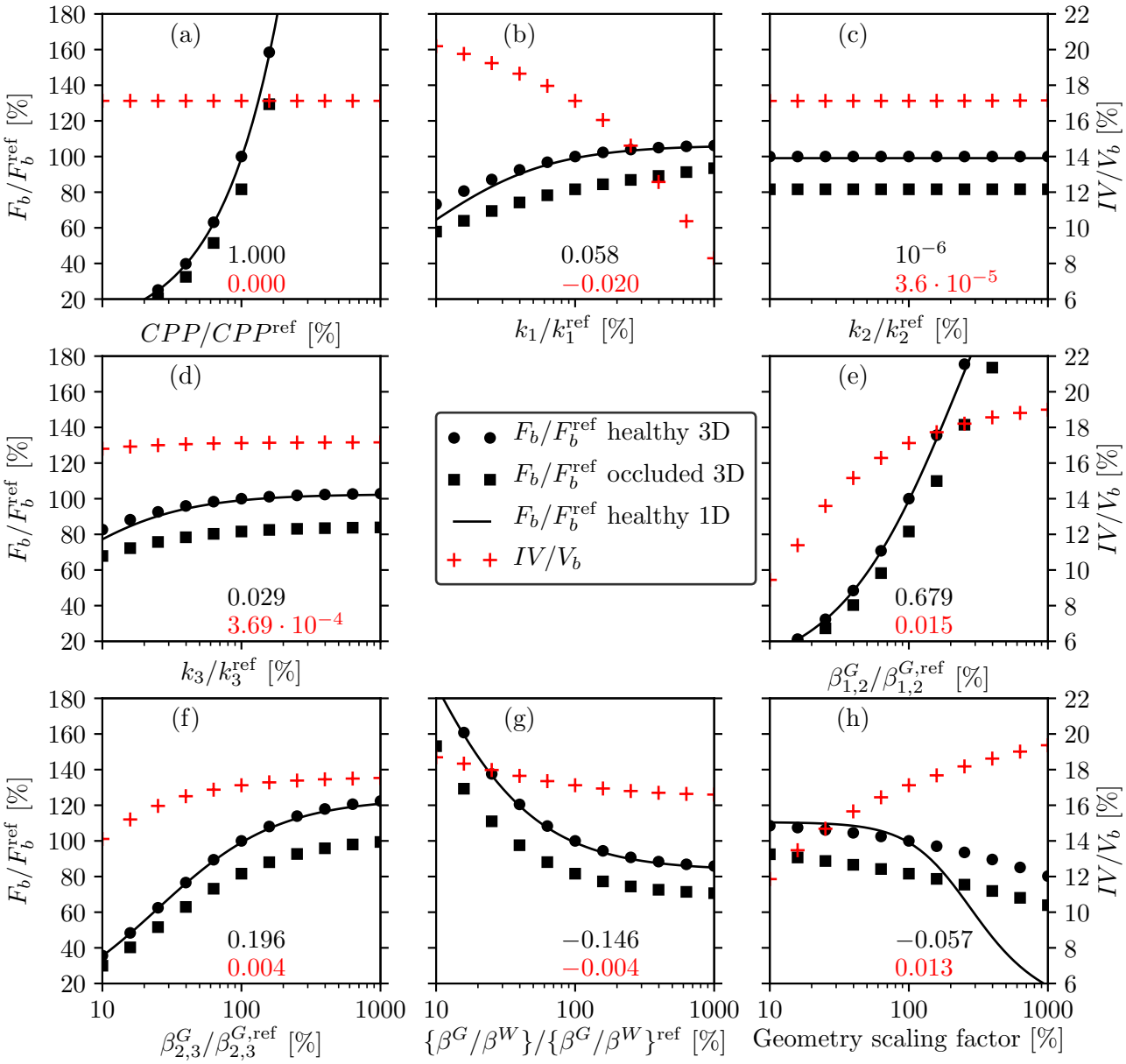

Figure 8: Sensitivity analyses of the 1D and 3D models. Brain perfusion (left axes) and infarcted volume fraction (right axes) as functions of change in the following parameters: cerebral perfusion pressure (a); arteriole (b), capillary (c), and venule (d) permeabilities; arteriole-capillary (e) and capillary-venule (f) coupling coefficients in the grey matter; ratio of grey and white matter coupling coefficients (g); geometry scaling factor (h). The top (black) and bottom (red) numbers on each subplot stand for the sensitivity of healthy brain perfusion and infarcted volume fraction, respectively. Reference values of the parameters are listed in Tab. 2.

Results are summarised in Fig. 8 showing brain perfusion as a function of the model parameters in the healthy scenario. Based on the 3D simulations, RMCA occlusion is also considered so that the perfusion in the occluded scenario and infarcted volume change are also displayed. Infarcted volume is estimated solely based on the perfusion distribution. A region with more than

bioRxiv preprint doi: https://doi.org/10.1101/2021.02.18.431511; this version posted February 18, 2021. The copyright holder for this preprint (which was not certified by peer review) is the author/funder, who has granted bioRxiv a license to display the preprint in perpetuity. It is made available under aCC-BY 4.0 International license.

70% perfusion drop compared to the baseline scenario is identified as an infarcted zone inspired by perfusion imaging-based methods [70, 71]. The obtained value estimating infarcted volume is used here solely as an indicator of perfusion drop severity because this method overestimates the ischaemic region compared to diffusion-weighted magnetic resonance imaging [72].

According to Figs. 8a-h, the 1D solutions follow the trend of the 3D simulations in a wide parameter range in every case except the geometrical scaling factor. Considering that the present 1D model does not account for curvature effects, the results could potentially be improved with a cylindrical or spherical formulation. The sensitivity of each parameter is estimated as the normalised partial derivative of brain perfusion and infarcted volume at 100% of the abscissa (around baseline values presented in Tab. 2). The derivatives computed based on the 3D simulations in Fig. 8a-h are listed above the abscissa and indicate the percentage change of brain perfusion and infarcted volume as a response to unit percentage change in model parameters.

In terms of haemodynamics, it should be noted that the present model captures solely the resistive part of the microcirculation and neglects conductance and inductance associated with vessel wall stiffness and pulsatility. The linear relationship between brain perfusion and perfusion pressure is a direct manifestation of the "hydraulic Ohm's law" (Fig. 8a). As other parameters are increased, brain perfusion tends to exhibit a saturating behaviour even if it is not obvious within the displayed parameter range (Fig. 8b-g) Considering the infarcted volume fraction, the insensitivity to CPP change originates from its definition restricted to relative perfusion change (as CPP is increased perfusion in the healthy and the occluded cases increases by the same amount).

Perturbations in the capillary and venous permeabilities have a relatively weak impact on both F_b and IV. In terms of the capillaries, this is a misleading behaviour which is a direct consequence of the structure of the brain model. Fluid flow within the capillary compartment is relatively small. This result can be interpreted as flow "avoiding" the capillaries because of their high resistance. Considering an indefinite domain with solely grey or white matter and constant but different arteriole and venous pressures, blood flow is non-zero between the compartments but it is zero inside each compartment. In the microcirculation, capillaries cannot be bypassed so it is important to recognise that the coupling coefficients must account not only for pre- and post-capillaries but also for the smallest capillary vessels. Therefore, the results show strong sensitivity to changes in coupling coefficients, which are responsible for the majority of the system resistance and consequently most of the pressure drop.

The geometry scaling factor has a strong influence on the infarcted volume fraction. If one of the major feeding arteries is occluded, it seems logical that for a given purely resistive vasculature a larger brain suffers more compared to a smaller brain. Such effects might be observable in clinical data but they are unlikely to be statistically significant compared to other factors, such as the extent of collateralisation. Nevertheless, the results suggest that a representative brain geometry is essential to keep the numerical uncertainty of the simulations low. In addition, the data presented in Fig. 8, and the one-dimensional model particularly, can help to accelerate virtual patient generation, where parameter sets must be found so that the resulting perfusion distribution is representative of a patient cohort.

3.4 Limitations

This subsection summarises some of the most important overlooked factors in the present study. Investigations are limited thus far to a single patient-specific brain geometry because of challenges associated with mesh generation. The porous model relies on multiple scale separation even though the vessel diameter in the vasculature changes continuously [20]. The present study demonstrated promising quantitative validation based on blood flow rate in major cere-

bioRxiv preprint doi: https://doi.org/10.1101/2021.02.18.431511; this version posted February 18, 2021. The copyright holder for this preprint (which was not certified by peer review) is the author/funder, who has granted bioRxiv a license to display the preprint in perpetuity. It is made available under aCC-BY 4.0 International license.

bral arteries but a more comprehensive validation is essential to ensure wider, multi-purpose applicability of the model.

The study is restricted to a porous model with three compartments (arteriole, capillary, venule) which are connected by homogeneous coupling coefficients both in grey and white matter. The model cannot represent arterioles which branch relatively far away from the cortical surface and hence feed deeper tissue regions. For this reason, low perfusion regions caused by occluded cerebral arteries are always connected to the brain surface so that isolated white matter infarction near the ventricles cannot be captured. On the one hand, such effects could be resolved by model expansion, for instance, by introducing two arteriole compartments which perfuse grey and white matter separately and rely on different boundary conditions. On the other hand, models with a single or two [22] compartments might be found more suitable in certain cases. Considering that the present study focuses on the sensitivity analysis of a three-compartment brain model for acute ischaemic stroke, exploring alternative porous frameworks for other specific (patho)physiological problems is left to future investigations.

From the haemodynamics point of view, the present model is purely resistive and aims to capture statistically steady state (time-averaged) brain perfusion. Therefore, the following physiological phenomena have been neglected: vessel wall stiffness (conductance), unsteady flow phenomena (inductance) [73], and cerebral autoregulation [74]. The associated processes and mechanisms are strongly time-dependent and often rely on nonlinear processes leading to significant complexity which is beyond the limits of the present study. Nevertheless, the authors hope that the present work will contribute to the creation of a comprehensive cerebral blood flow model which can incorporate these effects, in addition to pathophysiological processes, such as cerebral oedema [30], emboli advection and blockage of the microcirculation [53, 75, 76], and spreading of ischaemic tissue damage [77–79].

4 Conclusions

The present study set out to explore the sensitivity of a porous brain perfusion model and to prepare the ground for validation and uncertainty quantification. To this end, simulations were carried out using the finite element method and three test cases: a unit cube with manufactured solutions, a human brain geometry, and a one-dimensional brain tissue column. For the unit cube and the brain tissue column, analytical solutions were presented and used for verification. This approach allowed direct comparison between analytical and numerical results and enabled the identification of certain settings which were found crucial to minimise numerical errors.

The key findings of the study can be itemised as

- Blood pressure and perfusion can be estimated reasonably well on a relatively coarse grid and first order pressure elements.
- In order to approximate volumetric flow rate through superficial territories accurately with minimal computational effort, higher order finite elements are essential. Volumetric flow rate estimation can be further improved with local grid refinement in the vicinity of the superficial territories.
- Porous models can provide a good estimation of blood flow rate through major cerebral arteries when higher order elements and constant inlet pressure boundary conditions are used.
- Using uniform velocity inlet boundary conditions does not have solid physiological foundations because blood flow is likely not distributed proportionally to the cortical surface area. However, when considering healthy scenarios, constant pressure inlets can be prescribed with higher confidence.

bioRxiv preprint doi: https://doi.org/10.1101/2021.02.18.431511; this version posted February 18, 2021. The copyright holder for this preprint (which was not certified by peer review) is the author/funder, who has granted bioRxiv a license to display the preprint in perpetuity. It is made available under aCC-BY 4.0 International license.

- A multi-compartmental porous system can be solved analytically in one-dimensional cases. After determining the equivalent thickness of the subdomains, the one-dimensional system behaviour is representative of the three-dimensional organ-scale model. The one-dimensional case is suitable for parameter mapping and sensitivity analysis at a computational cost three orders of magnitude smaller compared to three-dimensional models.

The results lay down the foundations for validation, uncertainty quantification, and for the development of a multiscale model which incorporates large arteries as well as the microcirculation. The present work contributes to the creation of a reliable computational model which can assist in the design of clinical trials and in clinical decision making related to cerebrovascular diseases.

Acknowledgements

This work was funded by the European Union‘s Horizon 2020 research and innovation programme, the INSIST project, under grant agreement No 777072. Thanks are due to the members of the INSIST consortium for useful discussions and their sustained support.

Authors' contributions

TIJ carried out the research and prepared a draft of the manuscript under the supervision of SJP. RMP developed the brain territory clustering algorithm under the supervision of AGH. TIJ, WKE-B, and SJP designed the research and every author contributed to the revision of the paper.

Conflict of interest declaration

The authors declare that they have no conflict of interest.

Appendix A Whole brain model parametrisation

The baseline model parameters listed in Tab. 2 are determined using the method established in [14] as summarised below.

1. The capillary permeability k_2 and the venule-arteriole permeability ratio k_3/k_1 are assumed to be given based on previous studies [22, 51];

2. The ratio of the grey matter coupling coefficients ($\beta^G_{1,2}$ and $\beta^G_{2,3}$) can be calculated based on the spatially averaged pressure values in the grey matter ($\langle p_i \rangle^G$) using [14]

$$\frac{\beta^G_{1,2}}{\beta^G_{2,3}} = \frac{\langle p_2 \rangle^G - \langle p_3 \rangle^G}{\langle p_1 \rangle^G - \langle p_2 \rangle^G}. \tag{31}$$

   The ratio of the pressure drops is inferred from rodent experiments [67, 68]. Thereafter, both $\beta^G_{1,2}$ and $\beta^G_{2,3}$ can be calculated once the cerebral perfusion pressure is estimated [54] and grey matter perfusion $\langle F \rangle^G = \beta^G_{1,2}(\langle p_1 \rangle^G - \langle p_2 \rangle^G) = 56$ [ml/min/(100 ml)] is selected.

3. The remaining two parameters, namely k_1 and $\beta^G_{i,j}/\beta^W_{i,j}$, are obtained using optimisation [80, 81] relying on the minimalisation of the

$$J = (\langle F \rangle^G - \langle F \rangle^G_{\text{target}})^2 + (\langle F \rangle^W - \langle F \rangle^W_{\text{target}})^2 + J_{\text{penalty}} \tag{32}$$

bioRxiv preprint doi: https://doi.org/10.1101/2021.02.18.431511; this version posted February 18, 2021. The copyright holder for this preprint (which was not certified by peer review) is the author/funder, who has granted bioRxiv a license to display the preprint in perpetuity. It is made available under aCC-BY 4.0 International license.

cost function. The target perfuions in grey and white matter are set to physiologicall realistic values [82]: $F^G_{\text{target}} = 56$ and $F^W_{\text{target}} = 21$ [(ml blood)/min/(100 ml tissue)]. Furthermore, a penalty term (J_{penalty}) is applied to restrict the minimum and maximum perfusion values:

$$\begin{aligned} J_{\text{penalty}} =& H(F_{\text{min,target}} - F_{\text{min}}) \cdot (F_{\text{min}} - F_{\text{min,target}})^2 + \\ & H(F_{\text{max}} - F_{\text{max,target}}) \cdot (F_{\text{max}} - F_{\text{max,target}})^2. \end{aligned} \tag{33}$$

Here, H is the Heaviside function resulting in a non-zero J_{penalty} only if the extrema are out of the $F_{\text{min,target}} = 10$ and the $F_{\text{max,target}} = 80$ [(ml blood)/min/(100 ml tissue)] range.

References

[1] J. S. Rana, S. S. Khan, D. M. Lloyd-Jones, and S. Sidney. "Changes in Mortality in Top 10 Causes of Death from 2011 to 2018". In: *Journal of General Internal Medicine* (2020), pp. 1–2.

[2] D. S. Liebeskind. "Reperfusion for acute ischemic stroke: arterial revascularization and collateral therapeutics". In: *Current Opinion in Neurology* 23.1 (2010), pp. 36–45.

[3] P. S. S. Fransen et al. "MR CLEAN, a multicenter randomized clinical trial of endovascular treatment for acute ischemic stroke in the Netherlands: study protocol for a randomized controlled trial". In: *Trials* 15.1 (2014), p. 343.

[4] O. A. Berkhemer et al. "A randomized trial of intraarterial treatment for acute ischemic stroke". In: *New England Journal of Medicine* 372.1 (2015), pp. 11–20.

[5] D. J. Gladstone, S. E. Black, and A. M. Hakim. "Toward wisdom from failure - Lessons from neuroprotective stroke trials and new therapeutic directions". In: *Stroke* 33.8 (2002), pp. 2123–2136.

[6] M. Goyal et al. "Endovascular thrombectomy after large-vessel ischaemic stroke: a meta-analysis of individual patient data from five randomised trials". In: *The Lancet* 387.10029 (2016), pp. 1723–1731.

[7] C. Dargazanli et al. "Modified thrombolysis in cerebral infarction 2C/thrombolysis in cerebral infarction 3 reperfusion should be the aim of mechanical thrombectomy: insights from the ASTER trial (Contact Aspiration Versus Stent Retriever for Successful Revascularization)". In: *Stroke* 49.5 (2018), pp. 1189–1196.

[8] P. R. Konduri, H. A. Marquering, E. E. van Bavel, A. Hoekstra, C. B. L. M. Majoie, and the INSIST Investigators. "In-silico trials for treatment of acute ischemic stroke". In: *Frontiers in Neurology* 11 (2020), p. 1062.

[9] M. Viceconti, A. Henney, and E. Morley-Fletcher. "In silico clinical trials: how computer simulation will transform the biomedical industry". In: *International Journal of Clinical Trials* 3.2 (2016), pp. 37–46.

[10] A. G. Hoekstra, E. van Bavel, M. Siebes, F. Gijsen, and L. Geris. "Virtual physiological human 2016: translating the virtual physiological human to the clinic". In: *Interface Focus* 8 (2016).

[11] F. Pappalardo, G. Russo, F. M. Tshinanu, and M. Viceconti. "In silico clinical trials: concepts and early adoptions". In: *Briefings in Bioinformatics* 20.5 (2019), pp. 1699–1708.

[12] P. J. Blanco, L. O. Müller, and J. D. Spence. "Blood pressure gradients in cerebral arteries: a clue to pathogenesis of cerebral small vessel disease". In: *Stroke and Vascular Neurology* 2.3 (2017), pp. 108–117.

[13] R. M. Padmos, T. I. Józsa, W. K. El-Bouri, P. R. Konduri, S. J. Payne, and A. G. Hoekstra. "Coupling one-dimensional arterial blood flow to three-dimensional tissue perfusion models for in silico trials of acute ischaemic stroke". In: *Interface Focus* 11.1 (2021), p. 20190125.

[14] T. I. Józsa, R. M. Padmos, N. Samuels, W. K. El-Bouri, A. G. Hoekstra, and S. J. Payne. "A porous circulation model of the human brain for in silico clinical trials in ischaemic stroke". In: *Interface Focus* 11.1 (2021), p. 20190127.

[15] L. Guo et al. "Subject-specific multi-poroelastic model for exploring the risk factors associated with the early stages of Alzheimer's disease". In: *Interface Focus* 8.1 (2018), p. 20170019.

[16] L. Guo, Z. Li, J. Lyu, Y. Mei, J. C. Vardakis, D. Chen, C. Han, X. Lou, and Y. Ventikos. "On the validation of a multiple-network poroelastic model using arterial spin labeling MRI data". In: *Frontiers in Computational Neuroscience* 13 (2019), p. 60.

[17] J. C. Vardakis et al. "Fluid–structure interaction for highly complex, statistically defined, biological media: Homogenisation and a 3D multi-compartmental poroelastic model for brain biomechanics". In: *Journal of Fluids and Structures* 91 (2019), p. 102641.

bioRxiv preprint doi: https://doi.org/10.1101/2021.02.18.431511; this version posted February 18, 2021. The copyright holder for this preprint (which was not certified by peer review) is the author/funder, who has granted bioRxiv a license to display the preprint in perpetuity. It is made available under aCC-BY 4.0 International license.

[18] L. Guo, J. C. Vardakis, D. Chou, and Y. Ventikos. "A multiple-network poroelastic model for biological systems and application to subject-specific modelling of cerebral fluid transport". In: *International Journal of Engineering Science* 147 (2020), p. 103204.

[19] J. C. Vardakis, D. Chou, L. Guo, and Y. Ventikos. "Exploring neurodegenerative disorders using a novel integrated model of cerebral transport: Initial results". In: *Proceedings of the Institution of Mechanical Engineers, Part H: Journal of Engineering in Medicine* 234.11 (2020), pp. 1223–1234.

[20] M. Peyrounette, Y. Davit, M. Quintard, and S. Lorthois. "Multiscale modelling of blood flow in cerebral microcirculation: Details at capillary scale control accuracy at the level of the cortex". In: *PLoS ONE* 13.1 (2018), e0189474.

[21] W. K. El-Bouri and S. J. Payne. "Investigating the effects of a penetrating vessel occlusion with a multi-scale microvasculature model of the human cerebral cortex". In: *NeuroImage* 172 (2018), pp. 94–106.

[22] E. Hodneland et al. "A new framework for assessing subject-specific whole brain circulation and perfusion using MRI-based measurements and a multi-scale continuous flow model". In: *PLoS Computational Biology* 15.6 (2019), e1007073.

[23] C. Michler et al. "A computationally efficient framework for the simulation of cardiac perfusion using a multi-compartment Darcy porous-media flow model". In: *International Journal for Numerical Methods in Biomedical Engineering* 29.2 (2013), pp. 217–232.

[24] E. R. Hyde, C. Michler, J. Lee, A. N. Cookson, R. Chabiniok, D. A. Nordsletten, and N. P Smith. "Parameterisation of multi-scale continuum perfusion models from discrete vascular networks". In: *Medical & Biological Engineering & Computing* 51.5 (2013), pp. 557–570.

[25] E. R. Hyde et al. "Multi-scale parameterisation of a myocardial perfusion model using whole-organ arterial networks". In: *Annals of Biomedical Engineering* 42.4 (2014), pp. 797–811.

[26] J. J. Lee, E. Piersanti, K.-A. Mardal, and M. E. Rognes. "A mixed finite element method for nearly incompressible multiple-network poroelasticity". In: *SIAM Journal on Scientific Computing* 41.2 (2019), A722–A747.

[27] R. Willinger, H.-S. Kang, and B. Diaw. "Three-dimensional human head finite-element model validation against two experimental impacts". In: *Annals of Biomedical Engineering* 27.3 (1999), pp. 403–410.

[28] M. F. Horstemeyer, M. B. Panzer, and R. K. Prabhu. "State-of-the-art modeling and simulation of the brains response to mechanical loads". In: *Annals of Biomedical Engineering* 47.9 (2019), pp. 1829–1831.

[29] J. S. Giudice, W. Zeng, T. Wu, A. Alshareef, D. F. Shedd, and M. B. Panzer. "An analytical review of the numerical methods used for finite element modeling of traumatic brain injury". In: *Annals of Biomedical Engineering* 47.9 (2019), pp. 1855–1872.

[30] J. C. Vardakis, D. Chou, B. J. Tully, C. C. Hung, T. H. Lee, P.-H. Tsui, and Y. Ventikos. "Investigating cerebral oedema using poroelasticity". In: *Medical Engineering & Physics* 38.1 (2016), pp. 48 –57.

[31] M. Croci, V. Vinje, and M. E. Rognes. "Uncertainty quantification of parenchymal tracer distribution using random diffusion and convective velocity fields". In: *Fluids and Barriers of the CNS* 16.1 (2019), pp. 1–21.

[32] M. Croci, V. Vinje, and M. E. Rognes. "Fast uncertainty quantification of tracer distribution in the brain interstitial fluid with multilevel and quasi Monte Carlo". In: *International Journal for Numerical Methods in Biomedical Engineering* 37.1 (2021), e3412.

[33] A. Saltelli, S. Tarantola, F. Campolongo, and M. Ratto. *Sensitivity analysis in practice: a guide to assessing scientific models*. Vol. 1. Wiley Online Library, 2004.

[34] *Assessing Credibility of Computational Modeling through Verification and Validation: Application to Medical Devices (V & V 40), 2018*. The American Society of Mechanical Engineers (ASME).

[35] T. J. R. Hughes. *The finite element method: linear static and dynamic finite element analysis*. Courier Corporation, 2012.

[36] A. Logg and G. N. Wells. "DOLFIN: Automated finite element computing". In: *ACM Transactions on Mathematical Software* 37.2 (2010), p. 20.

[37] A. Logg, K.-A. Mardal, and G. Wells. *Automated Solution of Differential Equations by the Finite Element Method: The FEniCS Book*. Vol. 84. Springer Science & Business Media, 2012.

[38] M. Alnæs et al. "The FEniCS project version 1.5". In: *Archive of Numerical Software* 3.100 (2015).

[39] H. A. Van der Vorst. "Bi-CGSTAB: A fast and smoothly converging variant of Bi-CG for the solution of nonsymmetric linear systems". In: *SIAM Journal on Scientific and Statistical Computing* 13.2 (1992), pp. 631–644.

[40] Y. Shapira. "Multigrid Algorithms". In: *Matrix-Based Multigrid*. Springer, 2003, pp. 61–67.

[41] P. J. Roache. "Code verification by the method of manufactured solutions". In: *Journal of Fluids Engineering* 124.1 (2002), pp. 4–10.

bioRxiv preprint doi: https://doi.org/10.1101/2021.02.18.431511; this version posted February 18, 2021. The copyright holder for this preprint (which was not certified by peer review) is the author/funder, who has granted bioRxiv a license to display the preprint in perpetuity. It is made available under aCC-BY 4.0 International license.

[42] J. Weickenmeier, M. Jucker, A. Goriely, and E. Kuhl. "A physics-based model explains the prion-like features of neurodegeneration in Alzheimers disease, Parkinsons disease, and amyotrophic lateral sclerosis". In: *Journal of the Mechanics and Physics of Solids* 124 (2019), pp. 264–281.

[43] D. Garcia-Gonzalez, J. Jayamohan, S. N. Sotiropoulos, S.-H. Yoon, J. Cook, C. R. Siviour, A. Arias, and A. Jérusalem. "On the mechanical behaviour of PEEK and HA cranial implants under impact loading". In: *Journal of the Mechanical Behavior of Biomedical Materials* 69 (2017), pp. 342–354.

[44] D. Garcia-Gonzalez et al. "Cognition based bTBI mechanistic criteria; a tool for preventive and therapeutic innovations". In: *Scientific Reports* 8.1 (2018), p. 10273.

[45] H. Si. "TetGen, a Delaunay-based quality tetrahedral mesh generator". In: *ACM Transactions on Mathematical Software* 41.2 (2015), p. 11.

[46] T. W. Okell, M. A. Chappell, M. E. Kelly, and P. Jezzard. "Cerebral blood flow quantification using vessel-encoded arterial spin labeling". In: *Journal of Cerebral Blood Flow & Metabolism* 33.11 (2013), pp. 1716–1724.

[47] N. S. Hartkamp, E. T. Petersen, J. B. De Vis, R. P. H. Bokkers, and J. Hendrikse. "Mapping of cerebral perfusion territories using territorial arterial spin labeling: techniques and clinical application". In: *NMR in Biomedicine* 26.8 (2013), pp. 901–912.

[48] D. F. R. Heijtel et al. "Accuracy and precision of pseudo-continuous arterial spin labeling perfusion during baseline and hypercapnia: a head-to-head comparison with ^{15}O H2O positron emission tomography". In: *NeuroImage* 92 (2014), pp. 182–192.

[49] H. J. M. M. Mutsaerts, J. W. van Dalen, D. F. R. Heijtel, P. F. C. Groot, C. B. L. M. Majoie, E. T. Petersen, E. Richard, and A. J. Nederveen. "Cerebral perfusion measurements in elderly with hypertension using arterial spin labeling". In: *PloS one* 10.8 (2015), e0133717.

[50] N. S. Hartkamp, E. T. Petersen, M. A. Chappell, T. W. Okell, M. Uyttenboogaart, C. J. Zeebregts, and R. P. H. Bokkers. "Relationship between haemodynamic impairment and collateral blood flow in carotid artery disease". In: *Journal of Cerebral Blood Flow & Metabolism* 38.11 (2018), pp. 2021–2032.

[51] W. K. El-Bouri and S. J. Payne. "Multi-scale homogenization of blood flow in 3-dimensional human cerebral microvascular networks". In: *Journal of Theoretical Biology* 380 (2015), pp. 40–47.

[52] L. Wahlbin. *Superconvergence in Galerkin finite element methods*. Springer, 2006.

[53] W. K El-Bouri, A. MacGowan, T. I. Józsa, M. J. Gounis, and S. J. Payne. "Modelling the impact of clot fragmentation on the microcirculation after thrombectomy". In: *bioRχiv* (2020).

[54] K. Malhotra et al. "Association of elevated blood pressure levels with outcomes in acute ischemic stroke patients treated with intravenous thrombolysis: a systematic review and meta-analysis". In: *Journal of Stroke* 21.1 (2019), p. 78.

[55] L. Zarrinkoob, K. Ambarki, A. Wåhlin, R. Birgander, A. Eklund, and J. Malm. "Blood flow distribution in cerebral arteries". In: *Journal of Cerebral Blood Flow & Metabolism* 35.4 (2015), pp. 648–654.

[56] H. K. Versteeg and W. Malalasekera. *An introduction to computational fluid dynamics: the finite volume method*. Pearson Education, 2007.

[57] C.-Y. Xing, T. Tarumi, J. Liu, Y. Zhang, M. Turner, J. Riley, C. D. Tinajero, L.-J. Yuan, and R. Zhang. "Distribution of cardiac output to the brain across the adult lifespan". In: *Journal of Cerebral Blood Flow & Metabolism* 37.8 (2017), pp. 2848–2856.

[58] A. M. Winkler, M. R. Sabuncu, B. T. T. Yeo, B. Fischl, D. N. Greve, P. Kochunov, T. E. Nichols, J. Blangero, and D. C. Glahn. "Measuring and comparing brain cortical surface area and other areal quantities". In: *NeuroImage* 61.4 (2012), pp. 1428–1443.

[59] M. A. Ikram, H. A. Vrooman, M. W. Vernooij, F. van der Lijn, A. Hofman, A. van der Lugt, W. J. Niessen, and M. M. B. Breteler. "Brain tissue volumes in the general elderly population: The Rotterdam Scan Study". In: *Neurobiology of Aging* 29.6 (2008), pp. 882–890.

[60] D. Song, K. Lee, E. H. Kim, Y. D. Kim, J. Kim, T.-J. Song, H. S. Lee, H. S. Nam, and J. H. Heo. "Value of utilizing both ASPECTS and CT angiography collateral score for outcome prediction in acute ischemic stroke". In: *International Journal of Stroke* 10.7 (2015), pp. 1018–1023.

[61] D. S. Liebeskind. "Collateral circulation". In: *Stroke* 34.9 (2003), pp. 2279–2284.

[62] C. Luo et al. "Collateral blood flow in different cerebrovascular hierarchy provides endogenous protection in cerebral ischemia". In: *Brain Pathology* 27.6 (2017), pp. 809–821.

[63] A. M. M. Boers et al. "Value of quantitative collateral scoring on CT angiography in patients with acute ischemic stroke". In: *American Journal of Neuroradiology* 39.6 (2018), pp. 1074–1082.

[64] P. Blinder, A. Y. Shih, C. Rafie, and D. Kleinfeld. "Topological basis for the robust distribution of blood to rodent neocortex". In: *Proceedings of the National Academy of Sciences* 107.28 (2010), pp. 12670–12675.

bioRxiv preprint doi: https://doi.org/10.1101/2021.02.18.431511; this version posted February 18, 2021. The copyright holder for this preprint (which was not certified by peer review) is the author/funder, who has granted bioRxiv a license to display the preprint in perpetuity. It is made available under aCC-BY 4.0 International license.

[65] P. Blinder, P. S. Tsai, J. P. Kaufhold, P. M. Knutsen, H. Suhl, and D. Kleinfeld. "The cortical angiome: an interconnected vascular network with noncolumnar patterns of blood flow". In: *Nature Neuroscience* 16.7 (2013), p. 889.

[66] A. Y. Shih et al. "Robust and fragile aspects of cortical blood flow in relation to the underlying angioarchitecture". In: *Microcirculation* 22.3 (2015), pp. 204–218.

[67] S. L. Harper and H. G. Bohlen. "Microvascular adaptation in the cerebral cortex of adult spontaneously hypertensive rats". In: *Hypertension* 6.3 (1984), pp. 408–419.

[68] A. H. Werber and D. D. Heistad. "Effects of chronic hypertension and sympathetic nerves on the cerebral microvasculature of stroke-prone spontaneously hypertensive rats". In: *Circulation Research* 55.3 (1984), pp. 286–294.

[69] F. Schmid, P. S. Tsai, D. Kleinfeld, P. Jenny, and B. Weber. "Depth-dependent flow and pressure characteristics in cortical microvascular networks". In: *PLoS Computational Biology* 13.2 (2017), e1005392.

[70] B. C. V. Campbell et al. "Endovascular therapy for ischemic stroke with perfusion-imaging selection". In: *New England Journal of Medicine* 372.11 (2015), pp. 1009–1018.

[71] T. G. Jovin et al. "Diffusion-weighted imaging or computerized tomography perfusion assessment with clinical mismatch in the triage of wake up and late presenting strokes undergoing neurointervention with Trevo (DAWN) trial methods". In: *International Journal of Stroke* 12.6 (2017), pp. 641–652.

[72] W. A. Copen, A. J. Yoo, N. S. Rost, L. T. Morais, P. W. Schaefer, R. G. Gonzalez, and O. Wu. "In patients with suspected acute stroke, CT perfusion-based cerebral blood flow maps cannot substitute for DWI in measuring the ischemic core". In: *PloS one* 12.11 (2017).

[73] M. Chappell and S. J. Payne. *Physiology for Engineers*. Springer, 2020.

[74] S. J. Payne. *Cerebral Blood Flow and Metabolism: A Quantitative Approach*. World Scientific, 2017.

[75] V. J. Marder et al. "Analysis of thrombi retrieved from cerebral arteries of patients with acute ischemic stroke". In: *Stroke* 37.8 (2006), pp. 2086–2093.

[76] F. Bajd and I. Sersa. "Mathematical modeling of blood clot fragmentation during flow-mediated thrombolysis". In: *Biophysical Journal* 104.5 (2013), pp. 1181 –1190.

[77] E. Ruppin, E. Ofer, J. A. Reggia, K. Revett, and S. Goodall. "Pathogenic mechanisms in ischemic damage: a computational study". In: *Computers in Biology and Medicine* 29.1 (1999), pp. 39–59.

[78] L. Vatov, Z. Kizner, E. Ruppin, S. Meilin, T. Manor, and A. Mayevsky. "Modeling brain energy metabolism and function: a multiparametric monitoring approach". In: *Bulletin of Mathematical Biology* 68.2 (2006), pp. 275–291.

[79] Y. Xue, W. K. El-Bouri, T. I. Józsa, and S. J. Payne. "Modelling the effects of cerebral microthrombi on tissue oxygenation and cell death". In: *bioRχiv* (2021).

[80] J. A. Nelder and R. Mead. "A simplex method for function minimization". In: *The Computer Journal* 7.4 (1965), pp. 308–313.

[81] C. Zhu, R. H. Byrd, P. Lu, and J. Nocedal. "Algorithm 778: L-BFGS-B: Fortran subroutines for large-scale bound-constrained optimization". In: *ACM Transactions on Mathematical Software)* 23.4 (1997), pp. 550–560.

[82] L. M. Parkes, W. Rashid, D. T. Chard, and P. S. Tofts. "Normal cerebral perfusion measurements using arterial spin labeling: reproducibility, stability, and age and gender effects". In: *Magnetic Resonance in Medicine* 51.4 (2004), pp. 736–743.